Published OnlineFirst June 28, 2017; DOI: 10.1158/0008-5472.CAN-17-0668

Integrated Systems and Technologies

Cancer Research

Highly Accurate Detection of Cancer *In Situ* with Intraoperative, Label-Free, Multimodal Optical Spectroscopy

Michael Jermyn[1,2,3], Jeanne Mercier[2], Kelly Aubertin[2,4], Joannie Desroches[2], Kirk Urmey[5], Jason Karamchandiani[6], Eric Marple[5], Marie-Christine Guiot[6], Frederic Leblond[2,4], and Kevin Petrecca[1]

Abstract

Effectiveness of surgery as a cancer treatment is reduced when all cancer cells are not detected during surgery, leading to recurrences that negatively impact survival. To maximize cancer cell detection during cancer surgery, we designed an *in situ* intraoperative, label-free, optical cancer detection system that combines intrinsic fluorescence spectroscopy, diffuse reflectance spectroscopy, and Raman spectroscopy. Using this multimodal optical cancer detection system, we found that brain, lung, colon, and skin cancers could be detected *in situ* during surgery with an accuracy, sensitivity, and specificity of 97%, 100%, and 93%, respectively. This highly sensitive optical molecular imaging approach can profoundly impact a wide range of surgical and noninvasive interventional oncology procedures by improving cancer detection capabilities, thereby reducing cancer burden and improving survival and quality of life. *Cancer Res; 77(14); 1–9. ©2017 AACR.*

Introduction

Treatment of solid cancers includes combinations of surgery, radiotherapy, and chemotherapy. In this scheme, surgery is a means to access tissue for diagnosis and is a cancer treatment via cytoreduction. Many studies have shown dramatic survival advantages by surgically minimizing the volume of cancers, including melanoma (1), brain (2), breast (3), and lung cancers (4). Otherwise, precancerous, cancerous, or normal tissue invaded by cancer cells remain (5–7). When these residual cells are not eradicated by adjuvant treatments, they give rise to recurrences. The volume of residual cancer following surgery negatively impacts overall survival (4, 8–12).

In situ cancer detection remains a clinical challenge because the interface between the cancer and normal tissue can be difficult to visually discern, or cancer cell invasion into normal tissue eliminates any interface. A striking and well-established example is the common metastases to brain that develop in lung cancer and melanoma patients. These cancers appear to have a clear interface with the brain during surgery, and thus, an apparent complete resection is often achieved. Yet, even when postoperative MRIs suggest that no cancer remains, these cancers almost always recur at that exact surgical margin unless adjuvant radiotherapy is delivered. There is thus an unmet clinical need in oncology for practical, innovative technologies that can make cancers "visible" *in situ* and in real-time so as to minimally disrupt workflow.

One strategy to make cancer visible is by using fluorescence-based approaches. In these, exogenous agents targeting oncogenic processes are delivered with the aims of selective uptake in all cancer cells and the detection of these agents during surgery. To date, the only fluorescence agents that have been used in human studies are indocyanine green, fluorescein, and 5-aminolevulinic acid during brain cancer surgery (13). Each of these, however, is limited by insufficient sensitivity and variable uptake as a result of the genomic and molecular heterogeneity of cancers.

Another strategy to detect cancer within tissues is to use optics-based label-free tissue interrogation techniques, such as optical coherence tomography (OCT), Raman spectroscopy (RS), intrinsic fluorescence spectroscopy (IFS), and diffuse reflectance spectroscopy (DRS). OCT provides microscopic structural imaging. It has been used to detect brain cancer based on optical attenuation (14). RS provides vibrational molecular information based on inelastic light scattering from molecular species, including amino acids, lipids, proteins, and nucleic acid. It has been used in a variety of surgical oncology applications by exploiting the differences between spectroscopic molecular information inherent in normal tissues and cancers such as breast cancer (15), bladder cancer (16), brain cancer (7), precancerous cervical lesions (17), and gastrointestinal cancer during endoscopy (18). IFS detects endogenous fluorophores, including enzymes, metabolic cofactors, amino acids, porphyrins, and structural proteins. IFS has been used to detect bronchopulmonary cancer (19), epithelial

[1]Montreal Neurological Institute and Hospital, Department of Neurology and Neurosurgery, McGill University, Montreal, Quebec, Canada. [2]Department of Engineering Physics, Polytechnique Montreal, Montreal, Quebec, Canada. [3]Thayer School of Engineering, Dartmouth College, Hanover, New Hampshire. [4]Centre de Recherche du Centre Hospitalier de l'Université de Montréal, Quebec, Canada. [5]EMVision LLC, Loxahatchee, Florida. [6]Division of Neuropathology, Department of Pathology, McGill University, Montreal, Quebec, Canada.

Note: Supplementary data for this article are available at Cancer Research Online (http://cancerres.aacrjournals.org/).

M. Jermyn and J. Mercier contributed equally to this article.

Corresponding Authors: Frederic Leblond, Polytechnique Montreal, CP 6079, Succ. Centre-Ville, Montreal, QC, H3C 3A7. Phone: 514-340-4711 (ext. 4740); Fax: 514-340-4787; E-mail: Frederic.Leblond@polymtl.ca; and Kevin Petrecca, Montreal Neurological Institute and Hospital, McGill University, 3801 University St., Montreal, QC, H3A 2B4. Phone: 514-398-2591; E-mail: Kevin.Petrecca@mcgill.ca

doi: 10.1158/0008-5472.CAN-17-0668

Published OnlineFirst June 28, 2017; DOI: 10.1158/0008-5472.CAN-17-0668

precancerous tissue (20), laryngeal cancer (21), and breast cancer (22). DRS provides information from tissue absorbers, including oxygenated and deoxygenated hemoglobin, lipids, water, cytochromes, and melanin (23–25). DRS has been used to detect cervical cancer (26), melanoma and nonmelanoma skin cancers (27), breast cancer (28), and colorectal metastases to liver (29).

In vivo RS has been shown to be a highly specific and sensitive cancer detection method for multiple pathologies with detection accuracy values usually limited to approximately 90% (7, 15–17, 30), while oncology applications using IFS and/or DRS have been similarly limited (26, 28, 29, 31). We hypothesized that IFS and DRS have the potential to synergistically complement the molecular information provided by RS to maximize cancer detection capability. To test this hypothesis, we developed an integrated cancer detection system that combines IFS, DRS, and RS. This system exploits inherent nonredundant biological markers, such as molecular species with specific fluorescence, absorption, and molecular vibrational signatures (23–25). To optimize the diagnostic potential of these subtle spectrally distributed differences in the combined spectroscopic data from all three methods, a hierarchical supervised machine learning algorithm was developed for multivariate analysis to evaluate the ability to distinguish normal tissue from cancer using the spectral data. We then tested the capabilities of this system *in situ* during surgery and show that it achieves high accuracy, sensitivity, and specificity.

Materials and Methods

System setup: RS, IFS, and DRS

The new surgical probe shown in Fig. 1 allows sequential acquisition of spectra associated with RS, IFS for two excitation wavelengths, and DRS following excitation with a broadband white-light source. All hardware components (light sources, filter wheel, and detectors) are controlled using a custom LabView (National Instruments) program. The hand-held probe allows RS, IFS, and DRS tissue interrogation. The fiber-optic probe (Emvision, LLC) is connected to the illumination and detection subassembly by a 3-m long fiberoptic cable and has a 2.1-mm outer diameter. Nine low hydroxyl content 300-μm core silica fibers are distributed around a central 272-μm core silica fiber used for RS tissue excitation at 785 nm. Of the nine circularly distributed fibers, seven are used for collecting RS scattered light. The reemitted signal passes through a ring-shaped notch filter to remove elastically scattered laser light. Furthermore, to minimize the impact of the Raman signal from the optical fibers, an in-line short-pass emission filter is used in front of the excitation fiber. Two of the nine outer fibers are used for IFS and DRS. A custom two-component lens is used at the tip of the probe to ensure excitation, and detection areas for all fibers exactly overlap, thus making RS, IFS, and DRS measurements spatially colocated with a 0.5-mm interrogation area. The seven RS fibers combine into a single optical connector to maximize signal-to-noise ratio, while the IFS/DRS fibers are associated with two connectors: one for excitation and one for detection.

The detection connector for RS is connected to a spectrograph composed of a diffraction grating combined with a high-resolution charge-coupled device (CCD) camera (ANDOR Technology). A 1 W, 785 nm spectrum stabilized near-infrared laser (Innovative Photonic Solutions) with adjustable power is used for RS excitation. Two light-emitting diodes (LED) of different wavelengths (365 and 455 nm) are used for IFS, and a 3 W broadband LED (470–850 nm) is used for DRS (Thorlabs, Inc.). Prior to entering the probe excitation fiber, the IFS light sources are filtered using a low-pass filter to minimize potential excitation light bleed-through into the detection fiber. A stepper motor optical switch (DiCon Fiberoptics, Inc.) allows sequential tissue excitation with the IFS wavelengths and the DRS source. IFS and DRS detection is

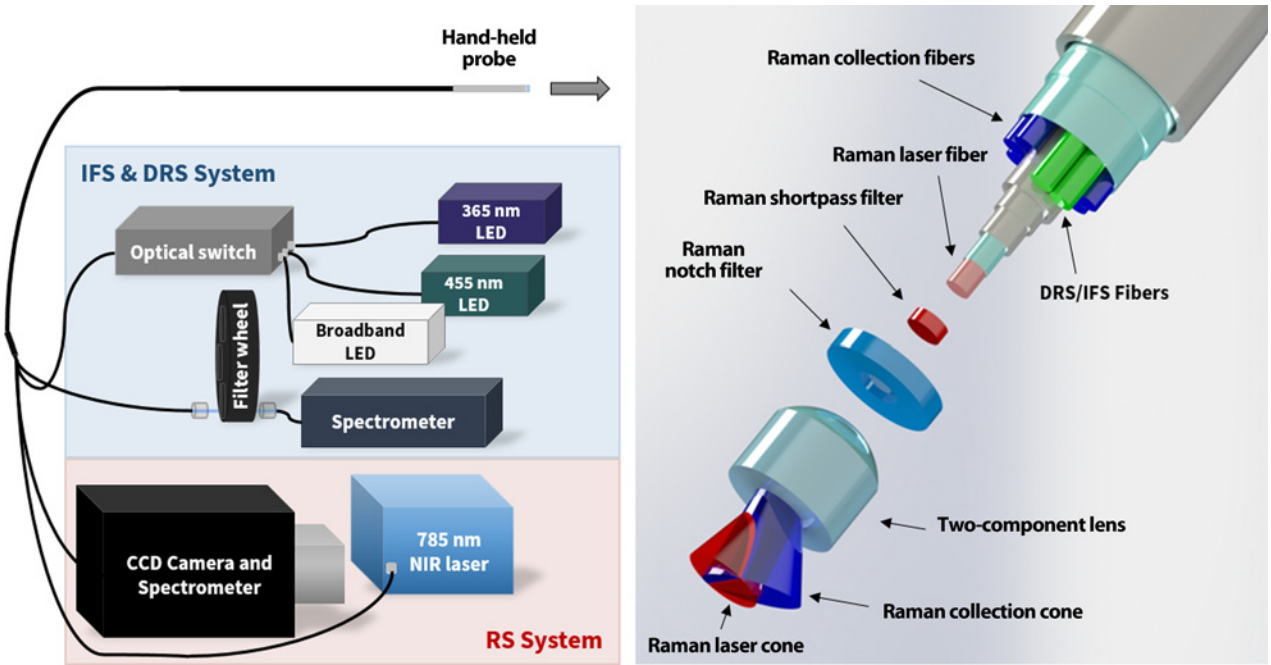

Figure 1.
System diagram for combined RS, IFS, and DRS. A single-point hand-held probe allows for corresponding acquisitions of the optical spectroscopy signals.

Published OnlineFirst June 28, 2017; DOI: 10.1158/0008-5472.CAN-17-0668

achieved using a compact spectrometer (Ocean Optics Inc.). A five-slot motorized filter wheel has been placed in the light path between the spectrometer and the IFS/DRS detection fiber of the probe. A long pass filter is used for the IFS channels selected to limit the amount of excitation light reaching the spectrometer. The sequential acquisition of each modality (RS, IFS, and DRS) is synchronized using the custom LabView program.

Intraoperative validation during brain tumor resection

This study investigated the use of RS, DRS, and IFS in a combined system using a handheld probe for intraoperative use on 15 adult patients undergoing open cranium surgery at the Montreal Neurological Institute and Hospital (Montreal, Canada). Patients with metastatic cancers and patients with grade 2–4 gliomas were selected. The study was approved by the Montreal Neurological Institute Ethics Review Board, and informed consent was obtained from all subjects. The methods were carried out in accordance with the approved guidelines and regulations. Standard clinical imaging by MRI was followed, as well as a complete preoperative neurologic examination.

During the study, the system was placed on a surgical cart and brought in the operating room (OR). It was then connected with the sterilized probe situated in the OR sterile zone. LabView program operation was performed by a member of the research group and the neurosurgeon operated the probe, blinded to any information relating to the acquired spectra during the resection procedure. An imaging sequence comprises background acquisition for RS, DRS, and IFS (system light sources turned off) and RS, DRS, and IFS acquisitions of tissue. Acquisitions on calibration standards were performed at the end of surgery to ensure normalization of the spectra can be achieved to remove contributions from the system response function. The neurosurgeon gave an assessment about the tissue imaged for each sample, based on tissue appearance through the surgical microscope and navigation guidance data, and collected a small biopsy sample ($\sim$3.5 mm^3) at the exact same position. Those samples were then embedded in paraffin and sent to histopathology for a standard blinded analysis using hematoxylin and eosin stain, performed by an expert neuropathologist. Using standard clinical practice, atypical cells were identified on the basis of their morphologic features, including nuclear atypia and nuclear polymorphism. Each sample was classified as either normal brain (no cancer cells present) or cancer. For analysis, all patients with grade 2–4 gliomas were pooled together, and all patients with metastatic cancers (lung, melanoma, and colon) were pooled together.

For each spectral acquisition, the microscope light was turned off temporarily. A Medtronic neuronavigation system (StealthStation) was used to locate the three-dimensional position of the probe relative to the preoperative MR images. This system uses small near-infrared (NIR) reflecting balls that are attached to the probe (SureTrack system, Medtronic) and an NIR light source. This source needs to be pointed away when the acquisition is made for RS because of the artifact it can create in the Raman spectra (32). Acquisition samples were rejected in the study if light artifacts were present in the signal, if CCD saturation was reached during the acquisition, or if the biopsy sample was partitioned (no homogeneity in the nature of the tissue).

Standard measurement time for the combined system is approximately 8 seconds. It includes one background acquisition for RS (integration time of 50 ms) and the three RS acquisitions (3 $\times$ 50 ms) that are averaged together for the analysis, plus the three background acquisitions (3 $\times$ 800 ms) and three acquisitions (3 $\times$ 800 ms) needed for DRS and IFS (one for each of the three light sources). Additional time is needed for the optical switch to go from one fiber to the other, for the filter wheel to move accordingly to the light source imaging at the time, and for the automated control via the LabView program. The output power at the end of the probe was measured using a powermeter, reporting 14.0 μW for the 455 nm source, 46.5 μW for the 365 nm source, and 0.5 μW for the white source. The output power for RS is typically 48 mW at the tip of the probe, but may vary between 27 and 75 mW to maximize the signal amplitude and avoid saturation.

Data analysis and tissue classification

Data preprocessing and calibration for IFS and DRS are described in detail in the Supplementary Methods. After these preprocessing steps, each IFS spectrum is normalized by the mean of the corresponding DRS spectrum, to correct for the effects of optical attenuation in tissue. Processing for RS involves background subtraction, correction by instrument response using measurements of a SRM2241 reference standard (National Institute of Standards and Technology, Gaithersburg, MD), the removal of intrinsic tissue fluorescence using an iterative polynomial fit (7), and standard normal variate normalization. Supervised machine learning methods can be used to distinguish different tissue types based on spectral characteristics, and a number of different methods have been used in previous studies such as support vector machines and linear discriminant analysis (33, 34). We previously demonstrated the efficacy of boosted trees for the classification of tissue based on Raman spectra (7), which operates by constructing an ensemble of decision trees that use differences in spectral information to distinguish different tissue types. This method was used here for RS tissue classification. For IFS, support vector machines were used for tissue classification, with feature selection based on the minimum redundancy maximum relevance (mRMR) method (35) to reduce the dimensionality of the spectra while retaining the most important information. When faced with multiple types of spectral information (here, RS and IFS), classifiers can be combined using hierarchical or sequential classification (36). In this case, we have employed hierarchical classification by using a classifier individually on the spectra from each of three datasets (RS, IFS – 365 nm, IFS – 455 nm), then combining the predictive information (posterior probabilities) from each classifier into a final support vector machines classifier. This allows us to use the multispectroscopy information to improve diagnostic capability. Leave-one-patient-out cross-validation (LOPO CV) was used to determine the accuracy, sensitivity, and specificity for the classification of RS alone, as well as for RS and IFS combined. LOPO CV treats all spectra from a single patient as the testing data, with spectra from all other patients as training data for the classifier. This process is repeated for each patient. This avoids potential bias caused by potential similarity of spectra from a single patient. Classification parameters such as the number of features used for mRMR and the number of decision trees for boosted trees were determined using cross-validation to achieve high sensitivity/specificity while avoiding overfitting to the data. In this study, all grades of gliomas were pooled, rather than classifying each grade individually. Sample size was chosen to achieve two-sided 95% normal-based confidence intervals of less than $\pm$5% for each of the classification results reported. All confidence interval calculations for

Published OnlineFirst June 28, 2017; DOI: 10.1158/0008-5472.CAN-17-0668

classification results were estimated using bootstrapping cross-validation.

Results

Cancer detection system design

The integrated optical cancer detection system was designed by combining IFS, DRS, and RS capabilities into a single hand-held probe coupled to a detection system (Fig. 1). The probe contains embedded fibreoptics for excitation and detection: one fiber for RS excitation; seven fibers for RS detection; one fiber for DRS/IFS excitation; and one fiber for DRS/IFS detection. A custom lens and filters are used to isolate the desired signals. The probe is connected to stimulating lasers, a CCD camera, and a spectrometer. All three modalities interrogate the same 500-μm diameter tissue region. Each *in situ* tissue interrogation requires a measurement time of approximately 8 seconds: 200 ms for RS; 2.4 seconds for DRS; and 2.4 seconds for each of the two IFS excitation bands.

Clinical testing design

We tested the performance of this system in a clinical study of patients harboring a variety of cancers, including primary brain cancers (gliomas), lung and colon cancers that had metastasized to brain, and melanoma that had metastasized to brain. During surgery, the probe was applied to normal and pathologic tissue regions and measurements were acquired for RS, DRS, and IFS. Ten to 15 sites were interrogated in each of the 15 patients included in the study for a total of 161 sites. Tissue was sampled at each site for blinded postinterrogation neuropathologic analysis to determine whether cancer cells were present in the interrogated region (Fig. 2A; Supplementary Fig. S1A). We then correlated these data with the corresponding processed spectral data (Fig. 2B; Supplementary Fig. S1B).

Tissue and spectral acquisitions

Neuropathologic analysis revealed that 69 of the trimodal measurements were acquired from normal brain, and 92 measurements were acquired from cancers or normal brain invaded by cancer cells (Table 1; Fig. 2A). RS, DRS, and IFS spectra for interrogation sites that contain dense cancer, normal brain invaded by cancer cells, and normal brain from a patient with a glioma are shown in Fig. 2B. For each tissue interrogation region, the spectroscopic information consisted of three spectra, totaling more than 1,600 spectral bands. The mean spectra for normal and cancer tissue for the entire cohort and for each modality (RS, IFS, and DRS) are shown in Fig. 3. The Raman spectra reveal molecular differences between normal and cancer tissue at the indicated peaks, associated with proteins, lipids, cholesterol, and nucleic acids. IFS spectra reveal subtle spectral distortions between tissues.

Cancer detection system performance

RS peaks were identified for lipids, nucleic acids, and cholesterol, as well as the three amide bands associated with the secondary structure of proteins (33, 37–43). The most significant biochemical differences between cancer and normal tissue were found, based on univariate statistical hypothesis testing of the individual RS peaks and tissue bands, as either increases (+) or decreases (−) in cancer. (Supplementary Table S1; Supplementary

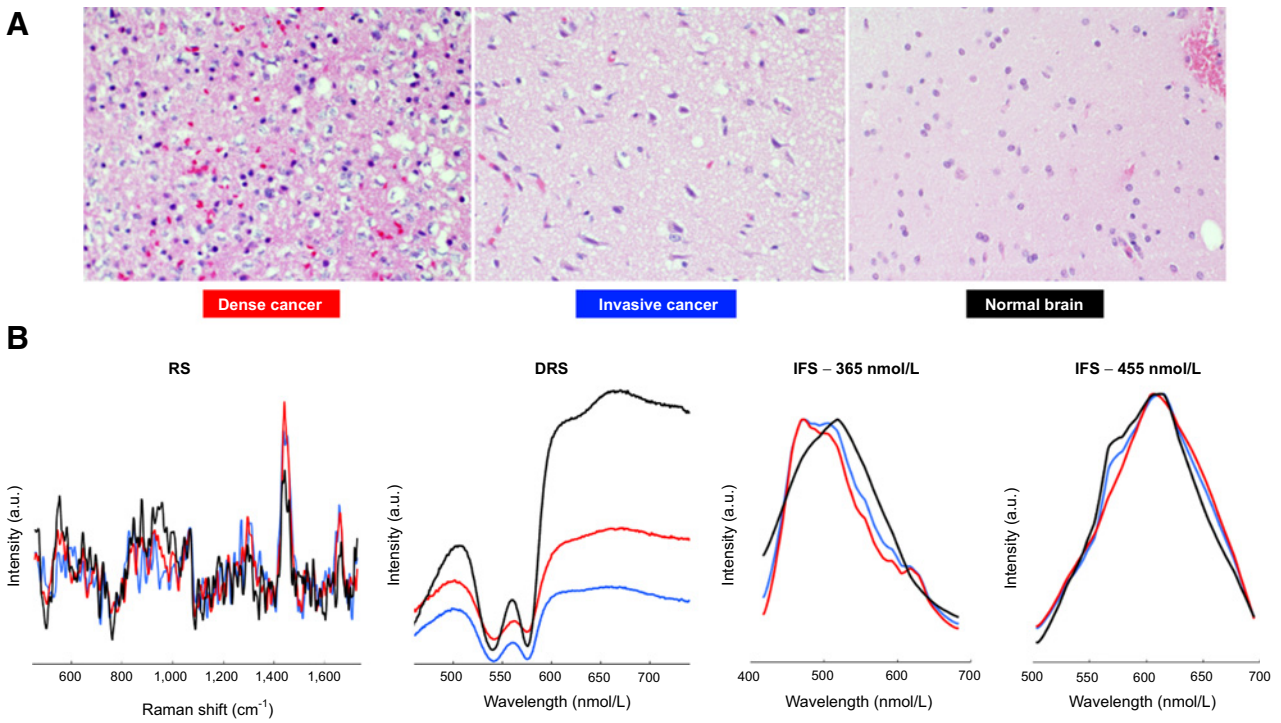

Figure 2.

A, Histopathology images (hematoxylin and eosin) are shown for three samples from a patient with a grade 2 oligodendroglioma, for dense cancer (left), invasive cancer (middle), and normal brain (right). **B,** The corresponding spectra obtained for each sample using RS, DRS, and IFS.

Published OnlineFirst June 28, 2017; DOI: 10.1158/0008-5472.CAN-17-0668

Table 1. Patient histologic diagnosis, indicating tumor grade and type as well as sample size information

			N patients	*N* samples
Brain cancer	Grade 2	Oligodendroglioma	1	9 (1)
	Grade 3	Oligodendroglioma	1	8 (8)
		Astrocytoma	2	34 (0)
	Grade 4	Glioblastoma	3	33 (23)
Lung cancer		Metastatic carcinoma	3	25 (23)
		Metastatic adenocarcinoma	3	28 (13)
Melanoma		Metastatic melanoma	1	13 (1)
Colon cancer		Metastatic adenocarcinoma	1	11 (0)
Total			$N = 15$	$N = 161$ (69)

NOTE: Metastatic cancers originated from the following primary sites: melanoma ($N = 1$), colon ($N = 1$), and lung ($N = 6$). The column for number of samples (N) also reports the number of normal tissue samples in parentheses.

Figs. S2 and S3). In particular, peaks correlating with DNA and RNA content were found to be higher for cancer, likely related to increased chromatin density (44, 45). Phospholipids and lipids, the main constituents of cell membranes and intracellular organelles, were more abundant in cancers because of the higher cell density in cancers compared with normal tissues. Amino acid, amide, and protein concentrations were also different, suggesting modifications in cellular functions such as metabolism (46), cell

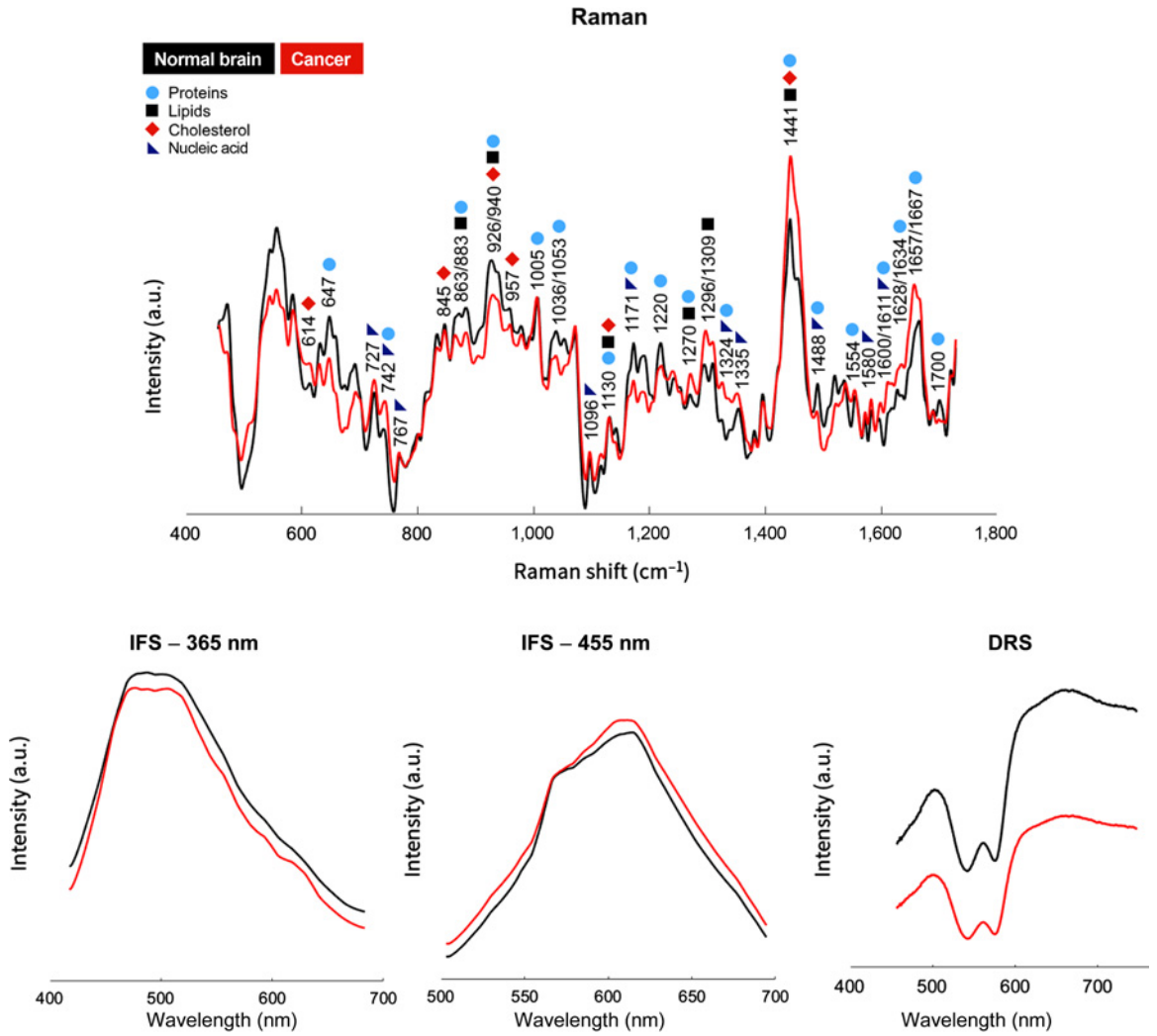

Figure 3.

The average spectra for RS, IFS, and DRS are shown for normal brain (black) and tissue containing cancer cells (red). Prominent Raman peaks are identified that are associated with proteins (light blue circle), lipids and phospholipids (black square), cholesterol/cholesterol esters (red diamond), and nucleic acids (dark blue triangle).

Published OnlineFirst June 28, 2017; DOI: 10.1158/0008-5472.CAN-17-0668

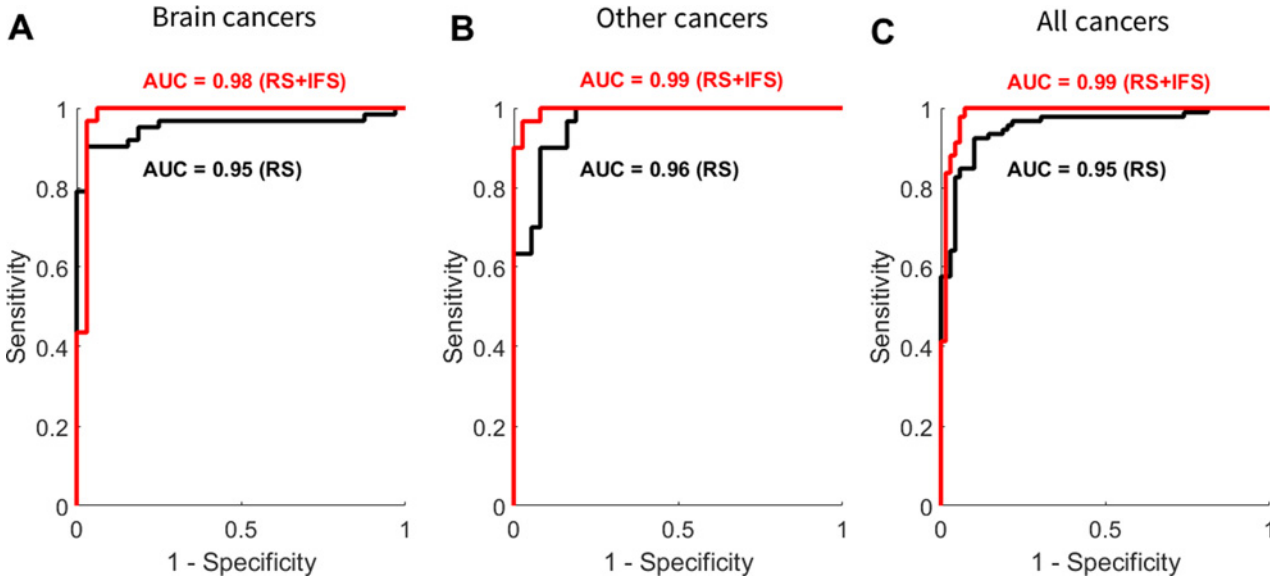

Figure 4.

ROC curve for distinguishing cancer tissue from normal brain using RS alone (black), or RS and IFS combined (red) in gliomas (**A**), metastasis (**B**), and metastases and gliomas combined (**C**). Corresponding AUC values are presented. See Table 1 for sample sizes.

migration (47), and neurotransmitter expression [phenylalanine (−), tryptophan (+/−), tyrosine (−), valine (−); ref. 48]. The expression of extracellular matrix components, such as proline (−), collagen (−), and elastin (−), was less in cancers (49).

The information associated with average IFS and DRS spectra is not as molecularly specific as RS because of the different physical origin of the light–tissue interaction processes leading to spectra with much less characteristic features. The spectra obtained for IFS and DRS conform to expectations and previous literature (26, 28, 29), as can be assessed on the basis of the shape of the intrinsic fluorescence spectra and the presence of characteristic hemoglobin peaks in the diffuse reflectance measurements (Fig. 3).

Spectra contain many features: peaks in the spectra; individual spectral points; or broader spectral shapes. To characterize the diagnostic potential of all spectra and individual features combined, multivariate statistical analysis was performed to automatically classify samples using a discriminative classifier given labeled training data based on a LOPO CV approach (see Materials and Methods). The classification results are reported using parametric ROC curves from which diagnostic accuracy figures can be derived. These are based on selecting the threshold parametric values providing optimal balance between sensitivity and specificity. ROC curves associated with tissue classification using RS or RS and IFS comparing normal brain and gliomas (Fig. 4A), normal brain and metastases (Fig. 4B), and normal brain with all cancers combined (Fig. 4C) show that in all instances the AUC is larger than or equal to 0.95. The AUC for RS and IFS combined is 0.98 for glioma detection and 0.99 for either the metastases or all cancers combined categories. The synergistic contribution of IFS to RS amounts to as much as 0.05 increases in AUC. The addition of IFS to RS can lead to a 5% increase in accuracy (93%–98%), a 10% increase in sensitivity (90%–100%), and 3% decrease in specificity (97%–94%) for gliomas (Table 2). Importantly, optimal tissue classification benefits are obtained when the full fluorescence spectroscopic information is used. The number of IFS spectral bands chosen by feature selection for tissue classification affects the classification accuracy of IFS. Feature selection chooses a subset of the spectral peaks, determining which individual points in the spectra are used for subsequent classification. Substantial performance improvements are observed for up to approximately 25 spectral bands of data, with moderate improvements thereafter (Supplementary Fig. S4).

Tissue classification using DRS combined with RS and IFS was valuable in normalizing the IFS data by mitigating the effect of optical attenuation from hemoglobin to ensure fluorescence data are minimally affected by intrinsic tissue absorption.

Table 2. Classification accuracy, sensitivity, and specificity for distinguishing cancer tissue from normal brain using RS alone, and using RS in combination with IFS (see Table 1 for sample sizes)

		Accuracy (%)	Sensitivity (%)	Specificity (%)
Gliomas	RS	93	90	97
	RS + IFS	98	100	94
Metastases	RS	90	97	84
	RS + IFS	96	100	92
All cancers combined	RS	91	92	90
	RS + IFS	97	100	93

Discussion

In situ cancer detection is profoundly important because residual cancer following surgery negatively influences the time to cancer recurrence and survival time. There is thus a need for the development of highly sensitive and specific cancer detection instruments that can be seamlessly integrated into clinical practice. Here, we report on the design, development, and clinical testing of an *in situ* intraoperative, label-free, optical cancer detection system that combines IFS, DRS, and RS. Using this multimodal optical cancer detection system, we found that solid cancers can be detected with extremely high accuracy and sensitivity. The AUC from ROC analysis demonstrated improvements by as much as 0.04 from 0.95 for standalone RS to 0.99 when combined with tissue fluorescence. This amounts to intraoperative cancer detection accuracies, sensitivities and specificities of 97%, 100%, and 93%, respectively. Improvements at the level reported here for all spectroscopy techniques combined become more important as sensitivity and specificity approach 100%, as it is indicative of approaching the threshold for complete resection and the associated survival benefits for many cancers. In this study, the spectral information from diffuse reflectance signals was normalized to fluorescence signals to attenuate the impact of intrinsic tissue absorption and scattering leading to spectral deformations specifically related to the presence of intrinsic fluorescent molecules.

One of the most profound findings was that the detection capabilities of the system were virtually unaffected by cancer type, indicating that this new multimodal machine learning classification technique can automatically classify tissue using the spectral features associated with the molecular characteristics of cancer. For example, we found that peaks and bands from Raman spectra correlated with molecular processes typically associated with cancer biology, including increased chromatin and nuclear volume, weakened immune response, and adaptation of the extracellular matrix to promote cell proliferation, cell migration, and angiogenesis.

Our results are exciting because the development and adaption of this novel technology is possible for a wide range of applications in open surgeries, minimally invasive laparoscopic, and robotic surgeries to detect cancer, cancer margins, and the cancer-normal tissue interface. This technology can also be used in other interventional oncology procedures, such as bronchoscopies and colonoscopies, to detect cancers that may not be visually obvious to the interventionalist and thereby increase the diagnostic accuracy of these procedures and treatments. Those potential applications are supported by the adaptive potential of the technology, which has already led to the development of wide-field imaging systems (50), submillimeter diameter surgical probes and optics-based biopsy needles.

The total imaging time of 8 seconds reported here can be potentially reduced by up to a factor of 10 by using more powerful LEDs for DRS and IFS, as light exposure levels used in this study are far below the maximum permissible tissue exposure in the visible region of the electromagnetic spectrum (ANSI Z136 Standards).

Future developments of our platform technology will involve testing in clinical trials designed to evaluate the robustness of the technique across a larger patient population and for a variety of cancer types. These will provide a substantial collection of spectra, which can then be used to assess the robustness of spectral features from the unique and differential molecular species. These trials will also be required to assess the effectiveness of this system using patient outcome metrics such as residual cancer following surgical intervention, diagnostic accuracy, progression-free survival, and overall survival.

Disclosure of Potential Conflicts of Interest

K. Urmey has ownership interest (including patents) in ODS Medical. E. Marple has ownership interest (including patents) in ODS Medical. F. Leblond is the co-founder (CTO) of and has ownership interest (including patents) in ODS Medical. K. Petrecca has ownership interest (including patents) in ODS Medical. No potential conflicts of interest were disclosed by the other authors.

Authors' Contributions

Conception and design: J. Mercier, K. Urmey, E. Marple, F. Leblond, K. Petrecca
Development of methodology: M. Jermyn, J. Mercier, J. Desroches, F. Leblond, K. Petrecca
Acquisition of data (provided animals, acquired and managed patients, provided facilities, etc.): M. Jermyn, J. Mercier, K. Aubertin, J. Desroches, J. Karamchandiani, M.-C. Guiot, K. Petrecca
Analysis and interpretation of data (e.g., statistical analysis, biostatistics, computational analysis): M. Jermyn, J. Mercier, K. Aubertin, J. Karamchandiani, M.-C. Guiot, F. Leblond, K. Petrecca
Writing, review, and/or revision of the manuscript: M. Jermyn, K. Aubertin, F. Leblond, K. Petrecca
Administrative, technical, or material support (i.e., reporting or organizing data, constructing databases): J. Desroches
Study supervision: F. Leblond, K. Petrecca
Other (histopathology): M.-C. Guiot

Grant Support

This work was supported by the New Researchers program from the Fonds de recherche du Québec - Nature et technologies (FRQNT), the Discovery Grant program from Natural Sciences and Engineering Research Council of Canada (NSERC), and the Collaborative Health Research Program (CIHR and NSERC). M. Jermyn was supported by postdoctoral fellowships from the Groupe de Recherche en Sciences et Technologies biomédicales (GRSTB), Banque Nationale, and FRQNT.

The costs of publication of this article were defrayed in part by the payment of page charges. This article must therefore be hereby marked *advertisement* in accordance with 18 U.S.C. Section 1734 solely to indicate this fact.

Received March 5, 2017; revised April 11, 2017; accepted April 27, 2017; published OnlineFirst June 28, 2017.

References

1. Hocevar M, Dragonja Z, Pilko G, Gazic B, Zgajnar J. Residual melanoma after an excisional biopsy is an independent prognostic factor for local recurrence and overall survival. Eur J Surg Oncol 2014;40:1271–5.
2. Stummer W, Reulen H-J, Meinel T, Pichlmeier U, Schumacher W, Tonn J-C, et al. Extent of resection and survival in glioblastoma multiforme: identification of and adjustment for bias. Neurosurgery 2008;62:564–76.
3. Bafford AC, Burstein HJ, Barkley CR, Smith BL, Lipsitz S, Iglehart JD, et al. Breast surgery in stage IV breast cancer: impact of staging and patient selection on overall survival. Breast Cancer Res Treat 2009;115:7–12.
4. Snijder RJ, Brutel de la Rivière A, Elbers HJ, van den Bosch JM. Survival in resected stage I lung cancer with residual tumor at the bronchial resection margin. Ann Thorac Surg 1998;65:212–6.

5. van der Toorn PP, Veltman JA, Bot FJ, de Jong JM, Manni JJ, Ramaekers FC, et al. Mapping of resection margins of oral cancer for p53 overexpression and chromosome instability to detect residual (pre)malignant cells. J Pathol 2001;193:66–72.
6. Agarwal A, Chang GJ, Hu C-Y, Taggart M, Rashid A, Park IJ, et al. Quantified pathologic response assessed as residual tumor burden is a predictor of recurrence-free survival in patients with rectal cancer who undergo resection after neoadjuvant chemoradiotherapy. Cancer 2013;119:4231–41.
7. Jermyn M, Mok K, Mercier J, Desroches J, Pichette J, Saint-Arnaud K, et al. Intraoperative brain cancer detection with Raman spectroscopy in humans. Sci Transl Med 2015;7:274ra19.
8. du Bois A, Reuss A, Pujade-Lauraine E, Harter P, Ray-Coquard I, Pfisterer J. Role of surgical outcome as prognostic factor in advanced epithelial ovarian cancer: a combined exploratory analysis of 3 prospectively randomized phase 3 multicenter trials: by the Arbeitsgemeinschaft Gynaekologische Onkologie Studiengruppe Ovarialkarzinom (AGO-OVAR) and the Groupe d'Investigateurs Nationaux Pour les Etudes des Cancers de l'Ovaire (GINECO). Cancer 2009;115:1234–44.
9. Chang S-J, Hodeib M, Chang J, Bristow RE. Survival impact of complete cytoreduction to no gross residual disease for advanced-stage ovarian cancer: a meta-analysis. Gynecol Oncol 2013;130:493–8.
10. Al-Rajhi N, Khafaga Y, El-Husseiny J, Saleem M, Mourad W, Al-Otieschan A, et al. Early stage carcinoma of oral tongue: prognostic factors for local control and survival. Oral Oncol 2000;36:508–14.
11. Stummer W, Meinel T, Ewelt C, Martus P, Jakobs O, Felsberg J, et al. Prospective cohort study of radiotherapy with concomitant and adjuvant temozolomide chemotherapy for glioblastoma patients with no or minimal residual enhancing tumor load after surgery. J Neurooncol 2012; 108:89–97.
12. Smith JS, Chang EF, Lamborn KR, Chang SM, Prados MD, Cha S, et al. Role of extent of resection in the long-term outcome of low-grade hemispheric gliomas. J Clin Oncol 2008;26:1338–45.
13. Stummer W, Pichlmeier U, Meinel T, Wiestler OD, Zanella F, Reulen H-J, et al. Fluorescence-guided surgery with 5-aminolevulinic acid for resection of malignant glioma: a randomised controlled multicentre phase III trial. Lancet Oncol 2006;7:392–401.
14. Kut C, Chaichana KL, Xi J, Raza SM, Ye X, McVeigh ER, et al. Detection of human brain cancer infiltration *ex vivo* and *in vivo* using quantitative optical coherence tomography. Sci Transl Med 2015;7:292ra100–292ra100.
15. Haka AS, Volynskaya Z, Gardecki JA, Nazemi J, Lyons J, Hicks D, et al. *In vivo* margin assessment during partial mastectomy breast surgery using Raman spectroscopy. Cancer Res 2006;66:3317–22.
16. Draga ROP, Grimbergen MCM, Vijverberg PLM, van Swol CFP, Jonges TGN, Kummer JA, et al. *Invivo* bladder cancer diagnosis by high-volume Raman spectroscopy. Anal Chem 2010;82:5993–9.
17. Mahadevan-Jansen A, Mitchell MF, Ramanujam N, Utzinger U, Richards-Kortum R. Development of a fiber optic probe to measure NIR Raman spectra of cervical tissue *in vivo*. Photochem Photobiol 1998;68:427–31.
18. Shim MG, Song LWK, Marcon NE, Wilson BC. *In vivo* near-infrared Raman spectroscopy : demonstration of feasibility during clinical gastrointestinal endoscopy. Photochem Photobiol 2000;72:146–50.
19. Zheng X, Xiong H, Li Y, Han B, Sun J. Application of quantitative autofluorescence bronchoscopy image analysis method in identifying bronchopulmonary cancer. Technol Cancer Res Treat 2016 July 19. [Epub ahead of print].
20. Georgakoudi I, Jacobson BC, Müller MG, Sheets EE, Badizadegan K, Carr-Locke DL, et al. NAD(P)H and collagen as *in vivo* quantitative fluorescent biomarkers of epithelial precancerous changes. Cancer Res 2002; 62:682–7.
21. Fostiropoulos K, Arens C, Betz C, Kraft M. [Noninvasive imaging using autofluorescence endoscopy: value for the early detection of laryngeal cancer]. HNO 2016;64:13–8.
22. Zhu C, Palmer GM, Breslin TM, Harter J, Ramanujam N. Diagnosis of breast cancer using fluorescence and diffuse reflectance spectroscopy: a Monte-Carlo-model-based approach. J Biomed Opt 2008;13:034015.
23. Jacques SL. Optical properties of biological tissues: a review. Phys Med Biol 2013;58:R37–61.
24. Weissleder R, Pittet MJ. Imaging in the era of molecular oncology. Nature 2008;452:580–9.
25. Ellis DI, Goodacre R. Metabolic fingerprinting in disease diagnosis: biomedical applications of infrared and Raman spectroscopy. The Analyst 2006;131:875–85.
26. Shaikh R, Prabitha VG, Dora TK, Chopra S, Maheshwari A, Deodhar K, et al. A comparative evaluation of diffuse reflectance and Raman spectroscopy in the detection of cervical cancer. J Biophotonics 2017;10:242–52.
27. Garcia-Uribe A, Zou J, Duvic M, Cho-Vega JH, Prieto VG, Wang LV. *In vivo* diagnosis of melanoma and nonmelanoma skin cancer using oblique incidence diffuse reflectance spectrometry. Cancer Res 2012;72: 2738–45.
28. Volynskaya Z, Haka AS, Bechtel KL, Fitzmaurice M, Shenk R, Wang N, et al. Diagnosing breast cancer using diffuse reflectance spectroscopy and intrinsic fluorescence spectroscopy. J Biomed Opt 2008;13:024012.
29. Tanis E, Evers DJ, Spliethoff JW, Pully VV, Kuhlmann K, van Coevorden F, et al. *In vivo* tumor identification of colorectal liver metastases with diffuse reflectance and fluorescence spectroscopy. Lasers Surg Med 2016;48: 820–7.
30. Crow P, Stone N, Kendall CA, Uff JS, Farmer JAM, Barr H, et al. The use of Raman spectroscopy to identify and grade prostatic adenocarcinoma in vitro. Br J Cancer 2003;89:106–8.
31. Evers DJ, Nachabe R, Vranken Peeters M-J, van der Hage JA, Oldenburg HS, Rutgers EJ, et al. Diffuse reflectance spectroscopy: towards clinical application in breast cancer. Breast Cancer Res Treat 2013;137: 155–65.
32. Desroches J, Jermyn M, Mok K, Lemieux-Leduc C, Mercier J, St-Arnaud K, et al. Characterization of a Raman spectroscopy probe system for intraoperative brain tissue classification. Biomed Opt Express 2015;6: 2380–97.
33. Kalkanis SN, Kast RE, Rosenblum ML, Mikkelsen T, Yurgelevic SM, Nelson KM, et al. Raman spectroscopy to distinguish grey matter, necrosis, and glioblastoma multiforme in frozen tissue sections. J Neurooncol 2014;116: 477–85.
34. Meyer T, Bergner N, Bielecki C, Krafft C, Akimov D, Romeike BFM, et al. Nonlinear microscopy, infrared, and Raman microspectroscopy for brain tumor analysis. J Biomed Opt 2011;16:021113.
35. Ding C, Peng H. Minimum redundancy feature selection from microarray gene expression data. J Bioinform Comput Biol 2005;3:185–205.
36. El-Shishiny H, Abdel-Mottaleb MS, El-Raey M, Shoukry A. A multistage algorithm for fast classification of patterns. Pattern Recognit Lett 1989;10: 211–5.
37. Bergner N, Krafft C, Geiger KD, Kirsch M, Schackert G, Popp J. Unsupervised unmixing of Raman microspectroscopic images for morphochemical analysis of non-dried brain tumor specimens. Anal Bioanal Chem 2012;403:719–25.
38. Beljebbar A, Dukic S, Amharref N, Manfait M. *Ex vivo* and *in vivo* diagnosis of C6 glioblastoma development by Raman spectroscopy coupled to a microprobe. Anal Bioanal Chem 2010;398:477–87.
39. Movasaghi Z, Rehman S, Rehman DIU. Raman spectroscopy of biological tissues. Appl Spectrosc Rev 2007;42:493–541.
40. Kast RE, Tucker SC, Killian K, Trexler M, Honn KV, Auner GW. Emerging technology: applications of Raman spectroscopy for prostate cancer. Cancer Metastasis Rev 2014;33:673–93.
41. Stone N, Kendall C, Smith J, Crow P, Barr H. Raman spectroscopy for identification of epithelial cancers. Faraday Discuss 2004;126:141.
42. Short KW, Carpenter S, Freyer JP, Mourant JR. Raman spectroscopy detects biochemical changes due to proliferation in mammalian cell cultures. Biophys J 2005;88:4274–88.
43. Vrabie V, Gobinet C, Piot O, Tfayli A, Bernard P, Huez R, et al. Independent component analysis of Raman spectra: application on paraffin-embedded skin biopsies. Biomed Signal Process Control 2007;2:40–50.
44. Matthäus C, Boydston-White S, Miljković M, Romeo M, Diem M. Raman and Infrared microspectral imaging of mitotic cells. Appl Spectrosc 2006;60:1–8.
45. Chan JW, Taylor DS, Zwerdling T, Lane SM, Ihara K, Huser T. Micro-raman spectroscopy detects individual neoplastic and normal hematopoietic cells. Biophys J 2006;90:648–56.
46. Weber G, Glazer RI, Ross RA. Regulation of human and rat brain metabolism: Inhibitory action of phenylalanine and phenylpyruvate on glycolysis, protein, lipid, DNA and RNA metabolism. Adv Enzyme Regul 1970;8: 13–36.

Published OnlineFirst June 28, 2017; DOI: 10.1158/0008-5472.CAN-17-0668

47. Toole BP. Hyaluronan: from extracellular glue to pericellular cue. Nat Rev Cancer 2004;4:528–39.
48. Platten M, Wick W, Van den Eynde BJ. Tryptophan catabolism in cancer: beyond IDO and tryptophan depletion. Cancer Res 2012;72:5435–40.
49. Lipinski CA, Tran NL, Bay C, Kloss J, McDonough WS, Beaudry C, et al. Differential role of proline-rich tyrosine kinase 2 and focal adhesion kinase in determining glioblastoma migration and proliferation1 1 national institutes of health grants HL67938 (J.C.L.) and NS42262 (M.E.B.). Mol Cancer Res 2003;1:323–32.
50. St-Arnaud K, Aubertin K, Strupler M, Jermyn M, Petrecca K, Trudel D, et al. Wide-field spontaneous Raman spectroscopy imaging system for biological tissue interrogation. Opt Lett 2016;41:4692–5.

Cancer Research
The Journal of Cancer Research (1916–1930) | The American Journal of Cancer (1931–1940)

AACR American Association for Cancer Research

Highly Accurate Detection of Cancer *In Situ* with Intraoperative, Label-Free, Multimodal Optical Spectroscopy

Michael Jermyn, Jeanne Mercier, Kelly Aubertin, et al.

Cancer Res Published OnlineFirst June 28, 2017.